ACS Catalysis

Research Article

pubs.acs.org/acscatalysis

Dramatic Effects of Gallium Promotion on Methanol Steam Reforming Cu−ZnO Catalyst for Hydrogen Production: Formation of 5 Å Copper Clusters from Cu−$ZnGaO_x$

Weiyi Tong,[†,‡,†] Adam West,[†] Kevin Cheung,[†] Kai-Man Yu,[†] and Shik Chi Edman Tsang*[,†]

[†]Wolfson Catalysis Centre, Department of Chemistry, University of Oxford, South Parks Road, Oxford, OX1 3QR, United Kingdom

[‡]Lab for Advanced Materials, Research Institute of Industrial Catalysis, East China University of Science & Technology, Meilong Road 130, Shanghai 200237, China

Supporting Information

ABSTRACT: A new class of copper, zinc, and gallium mixed oxides ($CuZnGaO_x$) with different chemical compositions obtained by a coprecipitation technique is identified as a highly active catalyst for the low-temperature, direct steam reforming of methanol to supply hydrogen gas to portable fuel cell devices. Their catalytic activity and selectivity are found to be critically dependent on the copper surface area, catalyst structure, and metal−support interaction, etc. As a result, temperature-programmed reduction has been used to investigate the copper ion reducibility and resulting copper speciation; N_2O chemisorption and advanced microscopies to determine specific copper surface area, dispersion, and particle size; XRD to investigate the catalyst structure; EPR spectroscopy to probe the environment of Cu^{2+} species; and AC impedance spectroscopy to probe the mobility of trapped ions in solids. It is proposed that Ga incorporation into Cu−Zn oxide leads to the formation of a nonstoichiometric cubic spinel phase containing interstitial Cu^{+} ions, which can produce in situ a high population of extremely small 5 Å copper clusters at high dispersion on a defective $ZnGa_2O_4$ surface for effective catalysis.

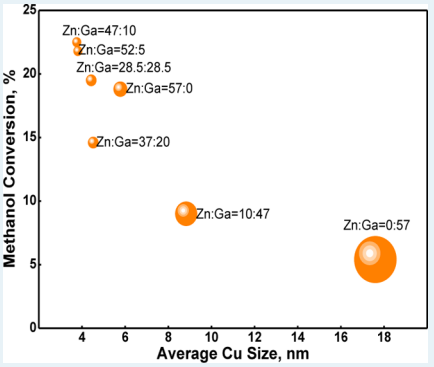

KEYWORDS: *H_2 production, fuel cells, methanol steam reforming, catalyst, particle size, gallium, copper clusters*

INTRODUCTION

Sustainable energy research has been the subject of intense global effort over recent years as concern has risen over declining fossil fuel reserves and their detrimental effect on the environment. In 1998, the Kyoto Protocol set out a legal agreement to reduce global CO_2 emissions to an average of 5.2% below 1990 levels by 2012.[1] In the U.K., the coalition government has set out to reduce greenhouse gas emissions to at least 34% below 1990 levels by 2020, reaching 80% reduction by 2050.[2] Clearly, to achieve these targets, alternative power sources will be required to meet our energy demands.

Hydrogen has long been considered the ideal environmentally friendly fuel because of its nonpolluting nature and high energy efficiency when used in a "proton-exchange membrane" (PEM) fuel cell. For portable applications (laptops, mobile phones, mp3 players, etc.), PEM fuel cells are considered to be even more energy-efficient than current Li ion battery technology.[3] This new hydrogen technology is therefore attracting significant interest around the world, not the least in the U.S.A., where research into PEM fuel cells for portable military applications is also ongoing.[4]

Hydrogen stored in a chemical form as liquid organic compounds and released in situ on demand at low temperature without CO contamination appears to be a more promising direction for mobile fuel cells. The primary liquid fuel can be stored in a disposable or recycled cartridge, which is changeable and logistically easily available. The generation of hydrogen from formic acid, which is nontoxic and a liquid at room temperature, with a density of 1.22 g mL^{-3}, has recently been demonstrated.[5] On the other hand, the direct use of methanol, which is a key platform chemical for existing fuel and chemical infrastructures and which has a high energy content of 5420 kcal kg^{-1}, is economically more attractive.[6,7] Thus, low-temperature direct steam reforming of methanol is regarded as a promising route to hydrogen production. It offers many advantages over other methods in terms of energy efficiency, CO mitigation, and safety considerations.[8] In a PEM fuel cell, the on-board steam reforming process can provide a source of hydrogen in situ (eq 1), which is then combined downstream with oxygen to produce water, with an accompanying release of energy:

$$CH_3OH + H_2O \rightleftharpoons 3H_2 + CO_2 \quad \Delta H^\circ = +49.7\ \text{kJ mol}^{-1} \tag{1}$$

$$2H_2 + O_2 \rightleftharpoons 2H_2O \quad \Delta H^\circ = -572\ \text{kJ mol}^{-1} \tag{2}$$

Received: January 3, 2013
Revised: March 5, 2013
Published: April 9, 2013

   dx.doi.org/10.1021/cs400011m | ACS Catal. 2013, 3, 1231−1244

CO gas could be formed via methanol decomposition or from a reversed water gas shift (RWGS) reaction:

$$CH_3OH \rightleftharpoons CO + 2H_2 \quad \Delta H^\circ = +90.2 \text{ kJ mol}^{-1} \quad (3)$$

$$CO_2 + H_2 \rightleftharpoons CO + H_2O \quad \Delta H^\circ = +41.2 \text{ kJ mol}^{-1} \quad (4)$$

CO production must be minimized as much as possible, since levels >10 ppm in the gas stream will poison noble-metal-based catalysts used in the downstream reaction (eq 2) and severely impair its performance.[9] By operating at reduced temperatures (150−200 °C) and with a suitable steam-reforming catalyst, this can be achieved directly without the need for complicated downstream multistage CO post-treatments. As a result, we have recently reported in a communication note that a reaction route for non-syn gas direct steam reforming of methanol for hydrogen production at low temperature can take place.[10] We have identified a new class of mixed oxides containing copper, zinc, and gallium as $CuZnGaO_x$, which are active and outperform 21 different types of Cu-based catalysts, including commercial steam reforming catalysts, with a hydrogen productivity of 393.6 mL-H_2/g-cat./h obtained with no CO formation at 150 °C in a contact time of 180 s kg-cat/mol. The results have showed high catalytic activity with no CO formation over the $CuZnGaO_x$ catalysts. It is particularly noted that the demand for hydrogen power in targeted small consumer devices is low (0.5−100 W), etc. As a result, we could afford to use lower temperatures, as low as 150 °C, and a higher water/methanol ratio for our catalyst studies, which would lower CO contents. According to our evaluation, the hydrogen productivity as demonstrated is feasible for small device applications.

Thus, in this study, further optimization of the catalyst formulation for hydrogen productivity has been carefully carried out. It is found that catalytic activity for steam reforming of methanol at 150−200 °C of this class of mixed oxides is critically dependent on copper particle size, catalyst structure, and metal−support interaction, etc. We also note an unusually high dispersion of copper on these mixed oxides with ∼5 Å copper cluster islands created on the surface of defective oxides upon their controlled reduction. It is attributed to the formation of a Cu ion-containing spinel phase when Ga^{3+} is incorporated in Cu/ZnO system, which produces a high population of ultrafine copper clusters with strong metal−support interaction (SMSI). This can suppress CO formation and enhance methanol conversion for effective catalysis at low temperature.

RESULTS

1. Thermodynamics. The methanol steam reforming reaction (MSR) consists of many elementary steps. To predict the extent of the reaction under defined conditions, the overall thermodynamics of the system must be considered. Figure 1 shows the thermodynamics predicted gaseous contents (CH_3OH, H_2, CO, CO_2, H_2O (not plotted); carbon deposition is not considered), which vary with temperature under reaction conditions with a 1:2 molar ratio of methanol and water.

As seen from Figure 1, H_2 and CO_2 are approaching stoichiometric production from methanol at nearly 100% conversion at 100−150 °C. The CO production stays close to zero before increasing exponentially when the temperature reaches above 200 °C (equilibrium of WGSR in eq 4 shifts forward). Therefore, to minimize CO production to prevent poisoning of downstream PEM fuel cell catalysts, MSR must be operated at reduced temperatures below 200 °C. However, at low temperature, the kinetics for CH_3OH conversion could be slow. Thus, a balance must be stuck between minimizing CO production and maximizing CH_3OH conversion for the direct supply of hydrogen gas to PEM fuel cells.

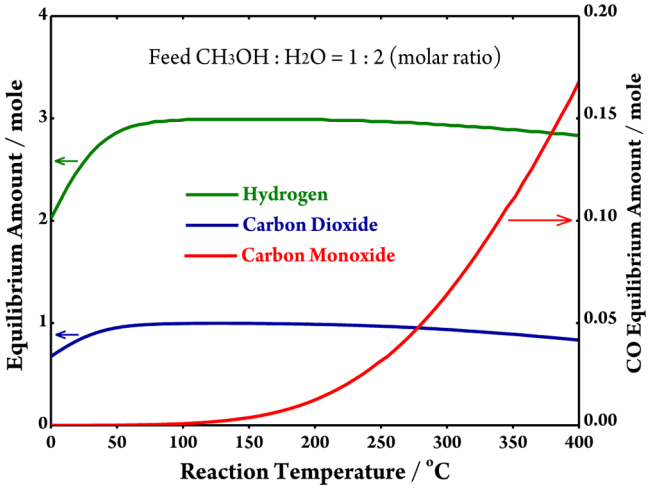

Figure 1. Thermodynamics equilibrium data of methanol steam reforming (CH_3OH/H_2O = 1:2).

2. Catalysis Testing. Table 1 shows a wide range of catalytic behavior over $CuZnGaO_x$ of different chemical composition (measured by inductive coupled plasma). The catalytic activity and selectivity in terms of methanol conversion and CO concentration are also given in the same table. The copper surface area per gram of catalyst (SA_{cat}), copper surface area per gram of Cu (SA_{Cu}), percent of copper dispersion (D_{Cu}), and average size of copper (X_{Cu}) were derived from N_2O chemisorptions (see the Experimental Section). It is clear from the Table that 43%Cu−$ZnGaO_x$ is the most active catalyst, achieving 33.4% CH_3OH conversion with a 108 ppm CO concentration at 195 °C.

To further disentangle the interplaying factors affecting the catalytic performance, contour maps of how these factors vary with the detailed Cu/Zn/Ga content of the catalysts were plotted.

As seen from Figure 2a, there is a clear "hot spot" at around 50% Cu, 30% Zn and 20% Ga, where the copper SA_{cat} is very high. Deviations from this formulation in any direction lead to a reduced specific surface area of Cu. Obviously, as the Cu content increases, we would expect the copper SA_{cat} to increase, but we observe that beyond ∼50% Cu loading, the surface area starts to decrease as a result of Cu sintering. It is thus clear that one important role of Zn or Ga is to keep the Cu particles effectively dispersed so they do not aggregate together upon calcination, leading to decreased particle size and increased surface area. It is noted that the incorporation of Zn to reduce Cu sintering has been long recognized in the literature.[6] Figure 2b is a contour map showing how CH_3OH conversion varies with atomic content. Here, we can see clearly the close correlation between the CH_3OH conversion and copper SA_{cat}, and once again, there is a hot spot around 50% Cu, 30% Zn, and 20% Ga. This is expected because copper metal provides the active sites at the interface with the support oxide for the MSR: a higher Cu surface area gives rise to a greater number of available sites.

Figure 3a is a contour plot showing how SA_{cat} affects CH_3OH conversion and CO production. This graph

dx.doi.org/10.1021/cs400011m | ACS Catal. 2013, 3, 1231−1244

Table 1. Summary of the Cu Dispersion and Size of Optimized Cu Catalysts Prepared under Coprecipitation at pH= 7 and Their Methanol Conversions and CO Concentrations at 195 °C

	atomic content (%)								
catalyst	Cu	Zn	Ga	CH_3OH conv (%)	CO (ppm)	D_{Cu} (%)	SA_{cat} ($m^2\ g^{-1}$)	SA_{Cu} ($m^2\ g^{-1}$)	X_{Cu} (nm)
15% Cu–$ZnGaO_x$	14.5	52.2	33.3	8.2	117	54.8	33.8	298.1	2.2
43%Cu–$ZnGaO_x$	48.7	31.3	20.0	33.4	108	24.6	76.7	214.0	3.6
60% Cu–$ZnGaO_x$	65.5	21.0	13.5	31.9	176	14.3	58.4	110.5	6.7
43%Cu–$ZnGaO_x$ (Zn/Ga = 3:2)	47.6	36.8	15.6	26.5	128	29.1	75.9	210.2	3.6
43%Cu–$ZnGaO_x$ (Zn/Ga = 1:3)	31.7	16.6	31.7	17.1	82	22.2	55.2	156.5	5.3

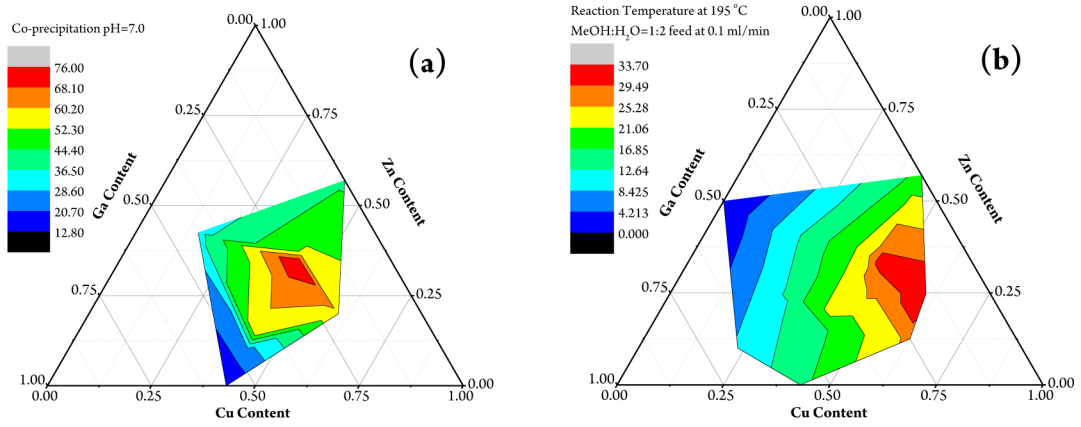

Figure 2. (a) Contour map showing variation of SA_{cat} (indicated by color gradient, units = $m^2\ g^{-1}$ cat.) with atomic content; (b) contour map showing variation of CH_3OH conversion (%) with atomic content at 195 °C.

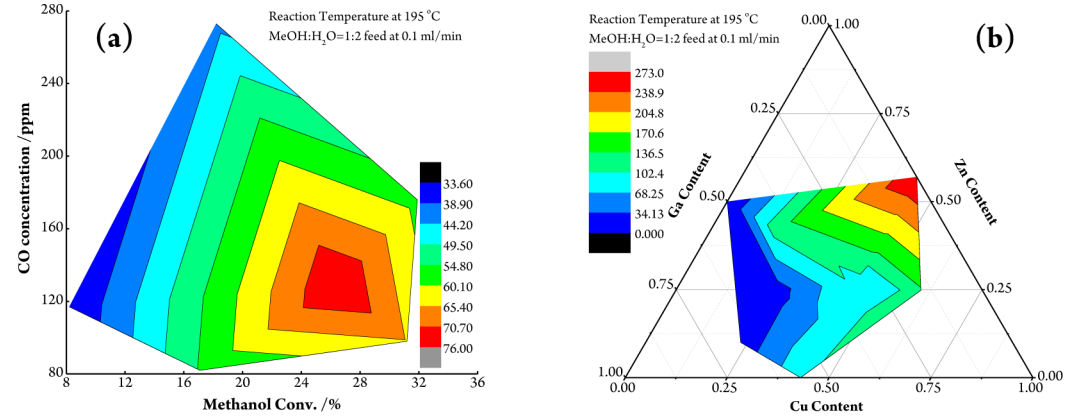

Figure 3. (a) Contour plot showing how SA_{cat} affects CH_3OH conversion and CO production; (b) contour map showing how CO production (ppm) varies with atomic content at 195 °C.

Table 2. Summary of the Cu Dispersion and Size of Optimized Cu Catalysts Prepared under Coprecipitation at pH= 6.5 and Their Methanol Conversions and CO Concentrations at 150 °C

	atomic receipe content (%)								
catalyst (code)	Cu	Zn	Ga	CH_3OH conv (%)	CO (ppm)	D_{Cu} (%)	SA_{cat} ($m^2\ g^{-1}$)	SA_{Cu} ($m^2\ g^{-1}$)	X_{Cu} (nm)
$CuZnO_x$	43	57	0	18.8	17	19.59	43.00	116.02	5.78
$CuZnGaO_x$ (A)	43	52	5	21.8	0	27.98	63.18	176.16	3.81
$CuZnGaO_x$ (B)	43	47	10	22.5	0	30.52	65.13	178.66	3.76
$CuZnGaO_x$ (C)	43	37	20	14.6	0	21.26	53.22	148.40	4.52
$CuZnGaO_x$ (D)	43	28.5	28.5	19.0	0	25.88	53.55	151.34	4.43
$CuZnGaO_x$ (E)	43	10	47	9.0	0	12.26	26.12	76.01	8.83
$CuGaO_x$ (F)	43	0	57	5.4	0	6.80	12.90	38.12	17.60
$CuZnAlO_x$	43	44	10 (Al)	12.61	12	16.71	47.30	131.87	5.09

demonstrates that, in general, CO production decreases as CH_3OH conversion increases, which is, in turn, critically dependent on the surface area of Cu (dispersion) in the catalyst. Therefore, it would appear that CO production could

dx.doi.org/10.1021/cs400011m | ACS Catal. 2013, 3, 1231–1244

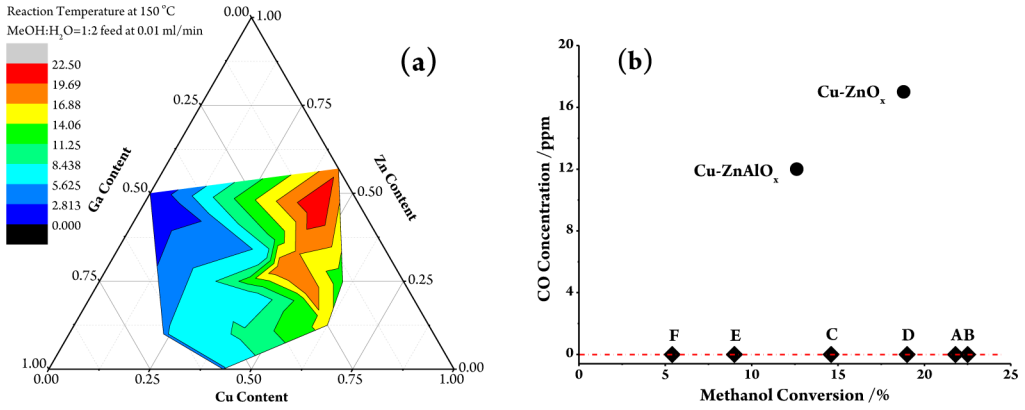

Figure 4. (a) Contour map showing variation of CH_3OH conversion (%) with atomic content; (b) methanol conversion against CO concentration at 150 °C under steam reforming conditions, reactant feeding at 0.01 mL/min.

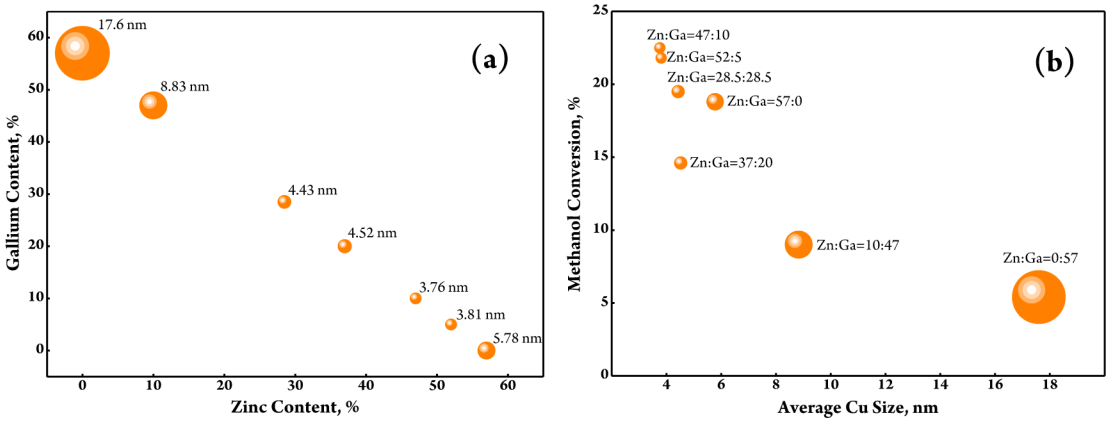

Figure 5. (a) Average copper size with different Zn/Ga content produced from 43%Cu−$ZnGaO_x$ (refer to Table 2) of different composition (total reduction to Cu^0); (b) corresponding methanol conversion at 150 °C.

be minimized simply by maximizing copper SA_{cat}. This would imply that the Zn/Ga oxide support plays no active role in the catalytic process itself and exists only to stabilize a highly dispersed, reducible form of Cu; however, Figure 3b, which shows how CO production varies with the catalyst formulation, indicates that this is not necessarily the case. The contour map in Figure 3b apparently shows that CO production is also strongly dependent on the Ga content, with CO levels decreasing as the Ga content is increased. This is an important and unique finding in this type of catalyst in the context of commercial $CuZnO_x$ catalysts without the Ga promoter. It appears that Ga in the support is playing an active role by enhancing the copper surface area (decrease in copper size) and somehow suppressing CO formation. It is known that addition of trivalent Ga^{3+} to M^{2+} (Cu^{2+}/Zn^{2+}) during coprecipitation would interlock the M^{2+} in a stable lattice to form a spinel structure (MGa_2O_4; see XRD) after heat treatment. It is interesting to note from Table 1 that using too high a ratio of Ga^{3+}/Cu^{2+} in 15% Cu−$ZnGaO_x$ (Ga^{3+}/Cu^{2+} = 2.3) and 43% Cu−$ZnGaO_x$ (Zn^{2+}/Ga^{3+} = 1:3; Ga^{3+}/Cu^{2+} = 1) can render the solids with lower CH_3OH conversions. Presumably, the reduction of structural Cu^{2+} in spinel is harder (needing a higher temperature for reduction than excess Cu^{2+} and under the conditions, sintering is taken place).

We then very carefully re-examined the synthesis of 43% Cu catalysts by coprecipitation at pH 6.5 to further reduce Cu particle sizes and enhance activities. Table 2 and Figure 4 show the Cu dispersions and sizes of the optimized Cu-based catalysts prepared from the coprecipitation method after the mild reduction and corresponding methanol conversions at a methanol/water molar ratio of 1:2 at 150 °C at shorter contact time (discourage eq 4). $CuZnGaO_x$ (B) is the most active catalyst, providing a decent methanol conversion of 22.5%. Interestingly, all six catalysts (A−F) containing Ga give no CO production (0 ppm), indicating that the addition of Ga indeed effectively minimizes CO production during the steam reforming of methanol at this low temperature (Figure 4b). On the other hand, without Ga addition, both $CuZnAlO_x$ and $CuZnO_x$ gave some activity for CO production; namely, 12 and 17 ppm, respectively. Again, using a higher ratio of Ga^{3+}/Cu^{2+} (≥1) the CH_3OH conversion decreases significantly at this low temperature (Table 2 and Figure 4a).

The $CuZnAlO_x$ catalyst has exactly the same atomic content as $CuZnGaO_x$ (B), except Ga is replaced by Al. The $CuZnGaO_x$ (B) catalyst out-performs the $CuZnAlO_x$ catalyst in both CO minimization and CH_3OH conversion optimization. This clearly suggests that although Ga and Al are trivalent ions, the Ga incorporation into the $CuZnO_x$ system can give a smaller copper particle size and lower CO production as well as enhanced CH_3OH conversion.

There is also a clear correlation between the Cu particle size and CH_3OH conversion tested at 150 °C over this type of catalyst. Both Cu dispersion and surface area increase as the particle size decreases: the increasing availability of active sites clearly enhances the overall conversion rate. The size of Cu particles depends mainly on their parent structure and

dx.doi.org/10.1021/cs400011m | ACS Catal. 2013, 3, 1231−1244

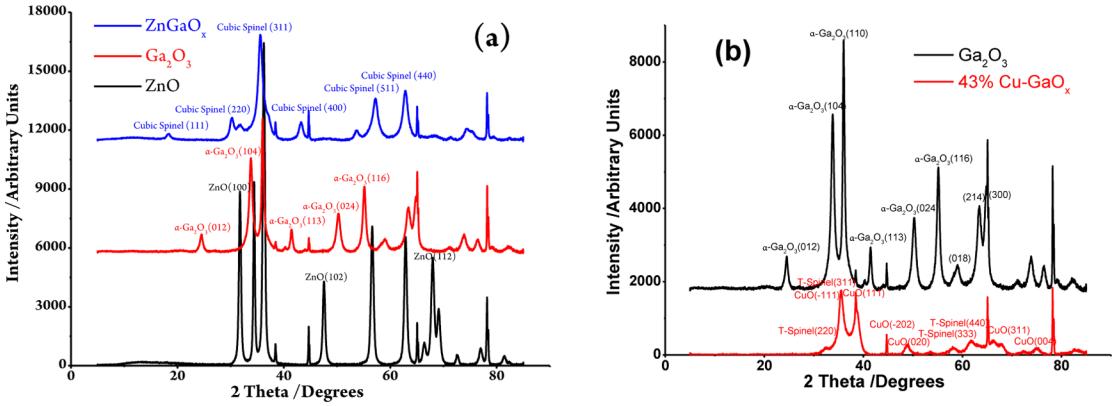

Figure 6. (a) XRD profiles of calcined ZnO (wurtzite), Ga_2O_3 (rhombohedral α-Ga_2O_3), and $ZnGaO_x$; (b) XRD profiles of calcined Ga_2O_3 and 43% Cu−GaO_x. The Al holder peaks as markers at 38°, 45°, 65°, and 78°.

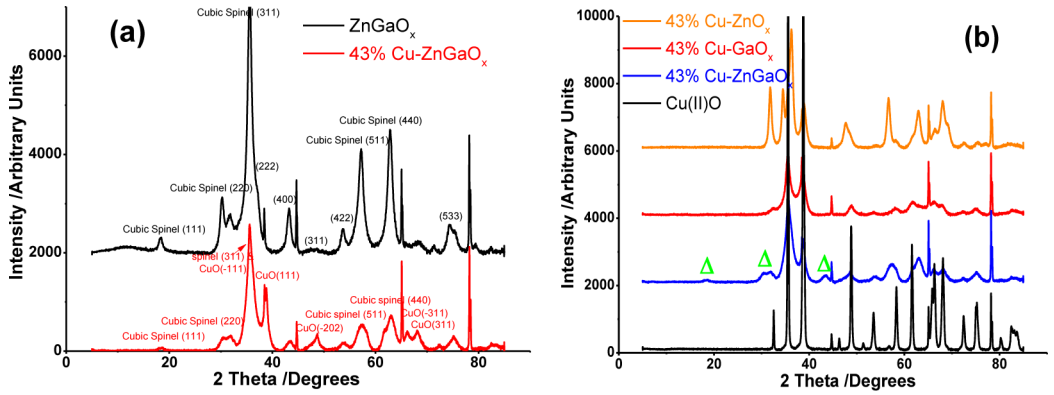

Figure 7. (a) XRD profiles of calcined $ZnGaO_x$ and 43%Cu−$ZnGaO_x$; (b) XRD profiles of calcined Cu containing samples prepared by coprecipitation. The cubic spinel phase of $ZnGa_2O_4$ substituted by Cu indicated by the green triangles is maintained. The Al holder peaks as markers at 38°, 45°, 65°, and 78°.

reducibility. Figure 5 demonstrates how the Cu particle size relates to the variation of Zn and Ga content.

In general, the $CuZnGaO_x$ structure gives a smaller copper particle size than the corresponding $CuZnO_x$, $CuGaO_x$, and $CuZnAlO_x$ at the same 43% loading, indicating that the addition of Ga^{3+} along with Zn^{2+} again has a significant impact on minimizing the Cu size, suppressing CO production and enhancing CH_3OH conversion. It would be important to correlate the structural changes associated with the Ga^{3+} incorporation with the above effects.

3. Structural Elucidations. *X-rays Powder Diffraction (XRD).* We first examined the formation of precipitate in the presence of Ga^{3+}, since a solid structure described as layered double hydroxides (LDHs) or hydrotalcite comprising layered materials with positively charged and charge-balancing anions located in the interlayer region can be favorably formed in the presence of trivalent cations. The LDHs are commonly represented by the formula $[M^{2+}_{1-x}M^{3+}_{x}(OH)_2]^{q+}(X^{n-})_{q/n}\cdot yH_2O$. Hence, the Ga^{3+} can form homogeneous solid LDH phase with either Cu^{2+} or Zn^{2+} in the catalyst precursors. We have, indeed, found that the hydrotalcite phase is clearly formed in the precipitate (see the Supporting Information). This could be related to our "hot spot" observed in catalysis. However, this solid precursor material is not thermally stable upon calcination (converted to spinel). Such a solid state relationship of hydrotalcite with respect to small Cu particles formation during calcination and reduction cannot be clearly deduced. XRD was then used to indicate the main working phase for each stable "calcined" catalyst studied. Note in Figure 6a that the majority of the diffraction peaks for calcined $ZnGaO_x$ can be indexed to a cubic spinel $ZnGa_2O_4$ structure,[11] with the wurtzite ZnO and α-Ga_2O_3 present as the minor phases. Thus, $ZnGaO_x$ prepared by coprecipitation consists of a heterogeneous mixture of cubic spinel $ZnGa_2O_4$ and minor Zn and Ga oxide phases after calcination.

It is also clear from Figure 6b that the presence of Cu significantly alters the α-Ga_2O_3 structure; the α-Ga_2O_3 phase is no longer present (readily forming a mixed phase with Cu^{2+}) in 43%Cu−GaO_x. The addition of Cu clearly triggers the formation of $CuGa_2O_4$ tetragonal spinel phase,[12] and excess CuO is also present. Thus, $CuGaO_x$ prepared by coprecipitation, consists of a heterogeneous mixture of tetragonal spinel $CuGa_2O_4$ and excess CuO phase after calcination.

As a result, it is clearly evident that Ga^{3+} incorporation would favor the formation of spinel phase with either Cu^{2+} or Zn^{2+} under the reaction conditions.

It is interesting to note that the XRD patterns of the most active 43%Cu−$ZnGaO_x$ catalyst closely resemble the peaks obtained for cubic spinel $ZnGa_2O_4$ instead of the tetragonal spinel $CuGa_2O_4$ (limited Ga^{3+} added appears to capture Zn^{2+} more favorably over Cu^{2+}), indicating that the predominant cubic spinel phase is maintained even upon the addition of a large quantity of Cu^{2+} (Figure 7a). However, it is important to note that some Cu ions may have substituted Zn^{2+} in the solid framework due to the similarity in their cation size (neighbor elements). For detailed comparison, there may be only traces of

dx.doi.org/10.1021/cs400011m | ACS Catal. 2013, 3, 1231−1244

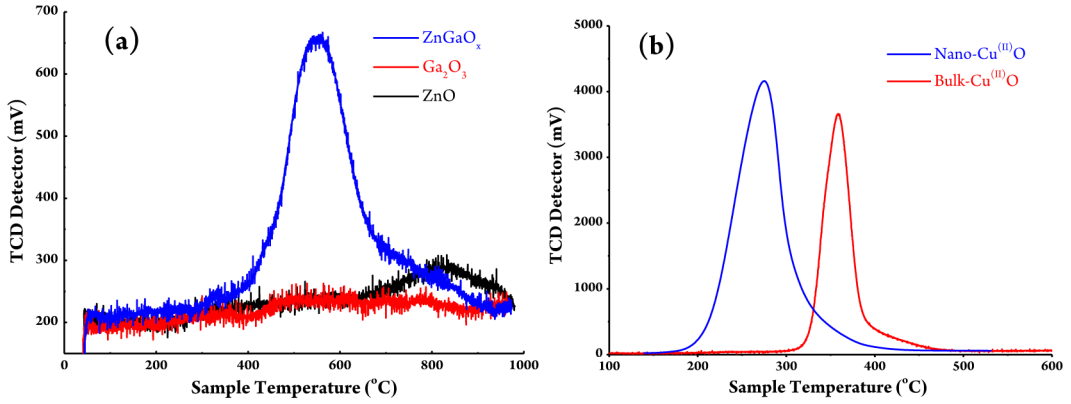

Figure 8. (a) TPR profiles for calcined ZnO, Ga_2O_3, and $ZnGaO_x$; (b) TPR profiles for 50 nm nano-Cu$^{(II)}$O and 300 nm bulk-Cu$^{(II)}$O.

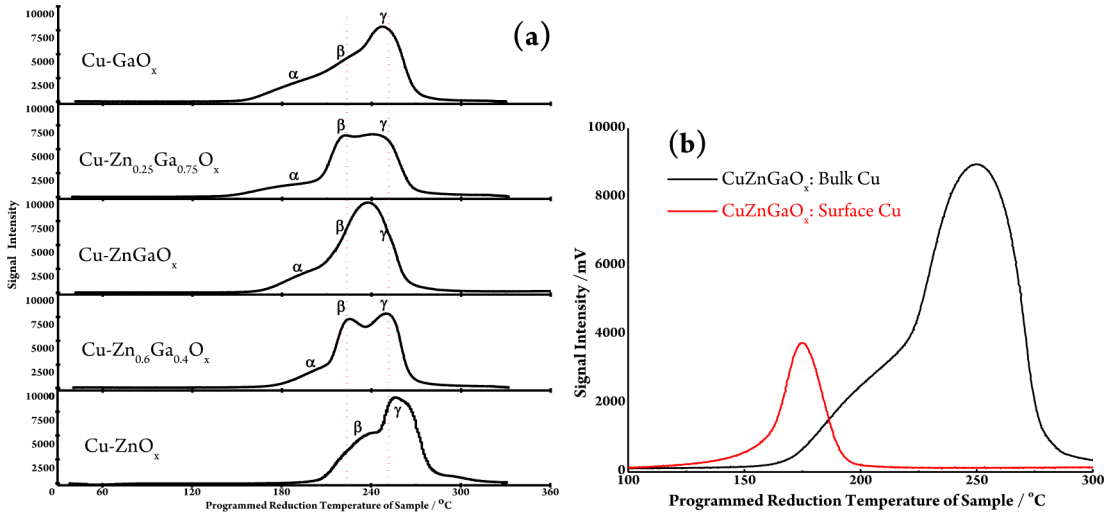

Figure 9. (a) Different Cu sizes (speciation) obtained from H_2-TPR reduction of $CuZnGaO_x$ oxides (refer to Table 1) and (b) TPR profiles for $CuZnGaO_x$ from Cu^{2+} and Cu^{+}.

the tetragonal spinel phase of $CuGa_2O_4$ in 43%Cu−$ZnGaO_x$, together with a Cu$^{(II)}$O phase (Figure 7b). Thus, the 43%Cu−$ZnGaO_x$ prepared by coprecipitation contains mainly the cubic spinel and traces of tetragonal spinel and CuO after calcination.

The CuO phase is apparently present as a significant part of a heterogeneous mixture in all the catalysts containing excess Cu prepared by coprecipitation, especially if the stoichiometry does not fit with the identified spinel phases (Figure 7b). Attempts were also carried out in collecting XRD patterns from a Diamond synchrotron source, UK (I11 synchroton XRD beam), but there were still peak overlaps between CuO (JCPDS No. 05-0661), spinel (JCPDS No. 44-0183) and other phases as a result of severe broadening of nanosize materials and poor quality of peaks, which were precluded from detailed refinements.

Nevertheless, when the spinel structure is calcined in a furnace, it can generate a significant number of oxygen defects, $Vo^{\bullet\bullet}$ at high temperature ($O^{2-} = Vo^{\bullet\bullet} + (1/2)O_2 + 2e^-$). Although such types of defective spinels are traditionally synthesized at much higher temperatures than our calcination temperature, their nanosizes with facilitated atom movement at extensive interfaces may still have been taking place. Since some cationic interstitial sites in the spinel structure are vacant, the migration and reduction of Cu^{2+} from CuO/spinel at the material interface can form a nonstoichiometric phase containing Cu^{+} in the interstitial sites of the spinel structure (see the Results Section), according to the literature.[13,14] However, using XRD, it is not easy to detect such a nonstoichiometric phase in a mixture of solid structures.

Temperature Programmed Reduction (TPR). Here, TPR has been used to investigate the Cu^{+} and Cu^{2+} reducibility and resulting copper speciation. Thus, TPR profiles of a range of Zn/Ga oxides with and without Cu were obtained over the temperature range 40−800 °C. Figure 8a first displays the TPR profiles of ZnO, Ga_2O_3, and $ZnGaO_x$ without the Cu addition.

Neither ZnO nor Ga_2O_3 (prepared from precipitation) are reduced in the temperature range, but $ZnGaO_x$ spinel with a more open structure (vacant interstitial sites) shows a small but significant reduction peak in hydrogen at ∼550 °C, which indicates the more facile reduction of Zn^{2+} species to Zn^{+} within the $ZnGaO_x$ spinel structure, which will be accompanied by the formation of oxygen vacancies. Similarly, at prolonged calcination, one would expect that the spinel structure can also generate oxygen vacancies at high temperature or under reducing conditions, with excess electrons to reduce cations or doper ions to form nonstoichiometric oxide, as discussed before.[13,14]

The TPR profiles of standard bulk and nano copper$^{(II)}$ oxides (CuO, Aldrich) with different particle sizes in Figure 8b were obtained over the temperature range of 40−600 °C. The nano-CuO, with an average particle diameter of 50 nm, shows a significant reduction peak at 280 °C, whereas the bulk-CuO,

dx.doi.org/10.1021/cs400011m | *ACS Catal.* 2013, 3, 1231−1244

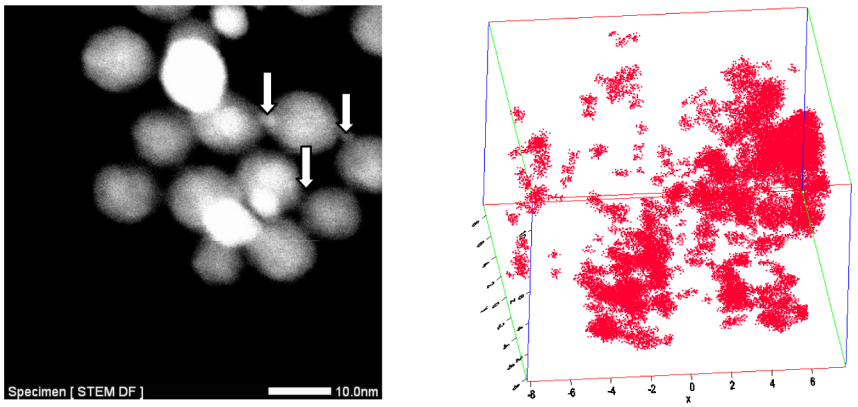

Figure 10. (a) HAADF-STEM image of $CuZnGaO_x$ catalyst after reduction showing a bimodal distribution of large Cu particles (7−9 nm) and small Cu clusters (∼0.5 nm, indicated by white arrows). (b) APT data of the specimen after reduction showing high-density pure Cu cluster areas in the solid matrix (red patches), units in nanometers.

with an average particle diameter of 300 nm, peaks at 370 °C. This indicates that the more facile reduction of Cu^{2+} species in the nano-CuO than in the bulk-CuO, presumably due to a higher degree of surface defective dominant features, with the nano-CuO starts reducing at 180 °C. Thus, the reducing temperature can be used to reflect the size of the Cu particles.

From Figure 9a, it is clear that there are three distinct Cu environments present in the Cu/Zn/Ga systems (labeled αCu, βCu, and γCu). αCu corresponds to the initial shallow reduction slope, which begins at a quite low temperature of ∼150 °C. βCu corresponds to the "kink" in the slope at ∼210 °C, rising to a maximum at 230 °C. γCu corresponds to the second maximum at 250 °C.

All the copper-containing solids give βCu and γCu peaks (producing smaller copper particle sizes than the standard 50 nm CuO when referencing to their reduction temperatures), but to a different extent, and the two peaks can sometimes be fused together. It is thought that both βCu and γCu peaks are formed as a result of reduction of framework Cu^{2+} from CuO and a mixed oxide matrix (more stable Cu^{2+} environment), respectively. Such reductions of framework Cu^{2+} are expected to give a similar activation energy; hence, they are reduced at a similar temperature regime. It is interesting to note that all the Ga-containing systems display an unique αCu peak, but 43% $Cu-ZnO_x$, containing no Ga, gives no αCu peak. As stated, this peak takes place at a much lower temperature (150 °C) than the other two peaks, indicating that it is unlikely to be caused by the reduction of Cu^{2+}, but rather, by more active Cu^+ in origin (the TPR peak is at around 150 °C for Cu^+ compounds; not shown). To verify this postulation, we employed N_2O chemisorption to reoxidize the Cu^0 produced from the first TPR reduction of $CuZnGaO_x$ (black line in Figure 9b) without exposure to air. It can be seen from the second TPR profile (red line in Figure 9b) of the N_2O reoxidized material (containing only Cu^+) in Figure 9b, which clearly shows that the reduction of Cu^+ takes place at ∼150 °C, reaching a maximum at 160 °C in the same solid matrix. This reduction peak of Cu^+ appears to match very well with the αCu shoulder peak. On the other hand, we do not have evidence to support the Cu^{2+} reduction can be taken place at such low temperature.

It is noted that $43\%Cu-ZnGaO_x$ shows the largest αCu peak amplitude, which gives the more superior catalytic activity for MSR evaluated at both 150 and 195 °C. We therefore attribute the αCu peak (reduced at 150 °C) to the reduction of interstitial Cu^+ species trapped in nonstoichiometric Ga spinel structure (refer to XRD). These Cu species with a lower oxidation state, lower neighbor atoms in the defective region (characterized by the highest mobility/reducibility) would expect to be reduced readily at the lowest temperature. Notice that $43\%CuGaO_x$ is easily reducible: the onset of reduction occurs earlier than any other catalyst. One might therefore have expected $43\%CuGaO_x$ to display a higher activity because of the formation of smaller copper particles produced (αCu peak) than the other catalysts, but the N_2O chemisorption in Table 1 suggested a different scenario (17.6 nm). As stated previously, it is essential to include Zn^{2+} in traditional methanol synthesis catalysts for textural dispersion of the copper phase; otherwise, copper is highly susceptible to sintering.[6] Although $CuGaO_x$ shows the presence of the low-temperature reduction shoulder in the TPR, the copper phase must have undergone a rapid sintering process to give large-size particles. Thus, a strong metal−support interaction is undoubtedly required to maintain the surface copper clusters formed from the solid structure.

Advanced Microscopies. High-angle annular dark field scanning transmission electron microscopy (HAADF-STEM) was used to acquire a detailed microscopic view of a typical $43\%Cu-ZnGaO_x$ catalyst particle after reduction. Using this imaging technique, an aberration-corrected transmission electron microscope revealed a significant number of copper particles (bright contrast) in the observable thin areas of the sample. The copper-rich particles ranged in size from ∼7 to 9 nm in diameter, as shown in Figure 10a. We believe that these Cu sizes correspond to βCu and γCu peaks because of a reduction of framework Cu^{2+}, as presented in Figure 9. Thus, the direct image of lattice fringes of these large Cu particles by bright field TEM is given in the Supporting Information. It is interesting to see from the HAADF-STEM image in Figure 10a that there are extremely small-sized copper clusters (0.5−2 nm) corresponding to an αCu peak produced from the reduction of Cu^+ (refer to Figure 9) in close proximity to the large Cu particles. Energy-dispersive X-ray spectroscopy confirmed that they were richer in Cu than the background, although the Cu content could not be unambiguously determined because of the resolution limit. However, we were unsuccessful in imaging the corresponding lattice fringes by bright field imaging for the small 0.5−2 nm Cu particles (expected to be more clusters than bulklike). To analyze the small Cu particles/clusters within the $CuZnGaO_x$ catalyst in further detail, we employed atom probe

dx.doi.org/10.1021/cs400011m | *ACS Catal.* 2013, 3, 1231−1244

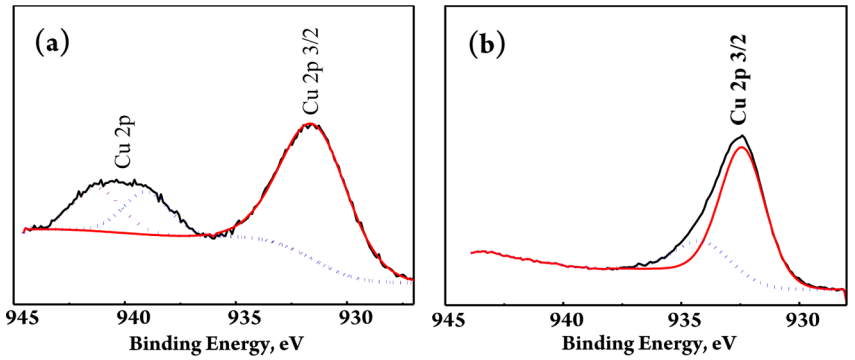

Figure 11. XPS study of Cu 2p 3/2 of $CuZnGaO_x$ catalyst (a) before reduction, 933.6 eV and two characteristic satellite peaks at 941.2 and 943.4 confirm the existence of Cu(II); (b) after reduction, sample (no satellite peak) contains typical bulk metallic Cu 2p 3/2 peak at 932.4 eV and also small Cu clusters peak at higher BE of 934.2 eV.[13].

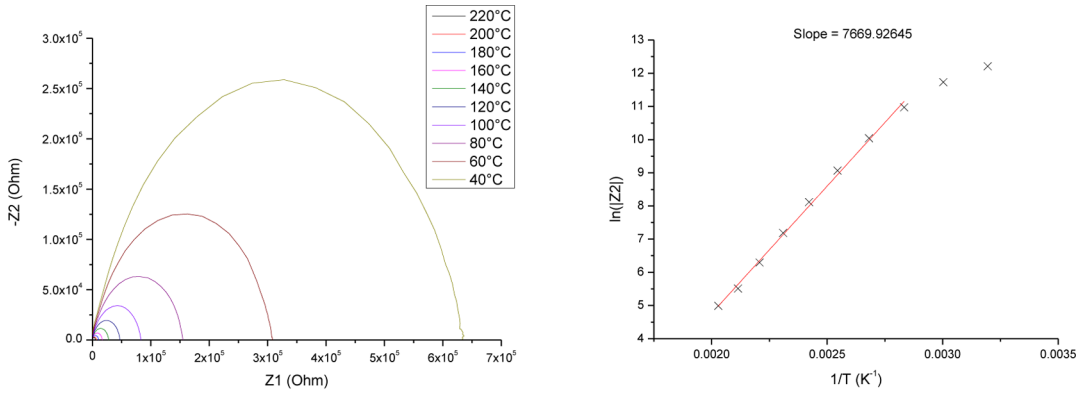

Figure 12. (a) Nyquist plot for 43%$CuZnGaO_x$; (b) Arrhenius plot for 43%$CuZnGaO_x$.

tomography (APT).[5,10] As shown in Figure 10b, there are Cu-rich regions. A closer examination of the copper atoms distribution in this region clearly reveals a high population of small copper-rich areas (copper clusters) of ~0.4−0.8 nm with 0.5 nm as the most probable mean size in close proximity to 6−8 nm Cu-rich particles. All these particles contained exclusively the Cu signal from mass spectroscopic analysis. Thus, the direct visualization by both the HADDF-STEM and APT discloses the bimodal distribution of large copper particles (from reduction of CuO and mixed oxide frameworks) together with very small copper clusters (from trapped Cu ions in spinel interstices).[10] As previously stated,[5,10] one should be cautious that there may be trajectory aberrations and artifacts induced by uneven evaporation of the sample during the APT analysis, which could lead to image blurring along the *z*-direction. Thus, a direct detailed comparison of size distribution between the two techniques should be carried out only with more experimental data.

XPS. After reduction, samples were carefully transferred in a glovebag without air exposure and analyzed by XPS. Figure 11 shows a binding energy study for the Cu 2p 3/2 peak of the $CuZnGaO_x$ catalyst before and after reduction.

In accordance with literature[15] XPS could be used to differentiate binding energy, BE of Cu 2p3/2 peak of a typical bulk metallic Cu phase at 932.4 eV from small copper clusters at 934.2 eV. Notice that there is indeed a clear shoulder on top of a typical bulk Cu peak in our sample after reduction as shown in Figure 11(b), at related shift direction, suggesting the presence of Cu clusters in the context of these literature values. In addition, there was no higher BE peak observed in the case of reduced $CuZnO_x$ (not shown). We can also rule out the possibility of reoxidation of Cu in glovebag as there was absolute clear region without the two characteristic satellite higher peaks at 941.2 and 943.4 eV of Cu ions. It is thus, evident that reduction of Ga spinel structure containing Cu interstitial ions can generate extremely small copper clusters in a parallel to relatively large Cu particles obtained through reduction of the framework Cu^{2+}.

AC Impedance. The AC impedance spectroscopy was used to assess electrical conductivity of a solid system. It is noted that the high mobility of interstitial ions (Cu^+ trapped) in a solid matrix can significantly contribute to the overall conductivity of the material instead of those framework ions. As a result, AC impedance spectra were obtained in air for a range of catalyst, and metal oxide materials, precalcined in air at 330 °C. The data obtained for each material are displayed in the form of a Nyquist plot, with the corresponding Arrhenius plot shown alongside, using the Z2 values measured at 10,000 Hz as an arbitrary point, which corresponds to the frequency at the top of the semicircles. These semicircles become increasingly smaller at higher temperatures, reflecting the rise in electrical conductivity that would be expected in a solid material containing mobile species. The Arrhenius plot of the cooling data yields a relatively straight line across the whole temperature range, indicating the validity of modeling the impedance via the Arrhenius equation. Figure 12a shows a typical result for 43%$CuZnGaO_x$ with high electrical conductivity (7000 Ωcm^{-2} at 200 °C with a low activation energy

dx.doi.org/10.1021/cs400011m | *ACS Catal.* 2013, 3, 1231−1244

of 0.661 eV derived from Figure12b), which indeed strongly indicates the presence of interstitial ions.

We note that the impedance results were far less stable (high impedance value >100,000 Ωcm^{-2} at 200 °C with activation energy >0.8 eV) for the non-Cu-containing oxides because of a lack of mobile species in these samples. In the cases of ZnO and Ga_2O_3, the Arrhenius plots were not linear across the desired temperature range. Nevertheless, an attempt was made to estimate their activation energy with the best straight line fitted in the range 200−220 °C (i.e., before deviation from Arrhenius behavior). For example, an activation energy of 1.1 eV corresponding well to the literature value of β-Ga_2O_3 was obtained.[16] Table 3 below summarizes the results for the AC impedance.

Table 3. AC Impedance Results Summary of Various Oxides and Mixed Oxides

catalyst	impedance (Z1) at 200 °C (Ωcm^{-2})	E_a (eV)	temp range (°C)
43% $CuZnGaO_x$	7000	0.661	80−220
43%$CuGaO_x$	14,000	1.102	120−220
ZnO	800,000	0.979	200−220
$ZnGaO_x$	$>10^6$	0.808	260−300
β-Ga_2O_3	$>10^6$	~1.1	167−300

From Table 3, it can be seen that the conductivity of the Cu-containing spinel materials is greatly enhanced by several orders of magnitude relative to their non-Cu analogues, with a concomitant lowering of the thermal activation energy. The value of impedance of CuO is not expected to be lower than ZnO (a typical conductivity of 2.5×10^{-10} Ωcm^{-2}); hence, we have ruled out its contribution to conductivity. On the other hand, the interstitial ions, such as Cu^+, associated with an oxygen defective region (missing oxygen sites) are expected to be mobile. This low impedance value and low activation energy can be attributed to the presence of mobile Cu^+ and $Vo^{\bullet\bullet}$ in the interstitial and oxygen-vacant sites, which act as the dominant charge carriers. For the non-Cu analogues, the dominant charge-carrying mechanism is likely via oxygen vacancies, but their activation energy for the migration of vacancy lattice defects is much higher than for mobile Cu ions.

Photoluminescence and Electron Paramagnetic Resonance Spectroscopy. To probe the defect concentration of the catalyst, the photoluminescence of the corresponding material was collected. Figure 13a shows the PL spectra of $CuZnGaO_x$ with an excitation wavelength of 350 nm, which clearly indicates the recombination of excitons taking place at higher wavelengths as a result of the presence of solid defects in the spinel structure. The concentrations of the defects appear to depend on the Zn/Ga ratios used, with 43%Cu−$Zn_{0.6}Ga_{0.4}O_x$ being the highest, followed by 43%Cu−$ZnGaO_x$. These solids, as demonstrated earlier, contain mobile copper species in the defective spinel structure (lower impedance, lower activation energy for mobility), which can be reduced easily to give superfine copper clusters. Thus, it is envisaged that their presence in the solids (interstitial copper ions and oxygen vacancies) gives the green emission at higher wavelength. It is interesting to note from Table 1 that they give the same average Cu particle size of 3.6 nm, but 43%Cu−$Zn_{0.6}Ga_{0.4}O_x$ with a higher Cu^{2+}/Ga^{3+} ratio appears to give a higher concentration of defects in the spinel structure, according to Figure 13a (hence, the smaller Cu particles). On the other hand, the higher content of Ga in 43%Cu−$ZnGaO_x$ should generate a higher spinel concentration in the solid matrix for a higher content of defect sites per gram basis. Their relative contribution to the overall average Cu size produced is not yet known.

Figure 13b shows the EPR spectra obtained with 43%Cu−ZnO_x, 43%Cu−$ZnGaO_x$, and 43%Cu−GaO_x. It is noted that 43%Cu−ZnO_x displays a strong, sharp signal at 3500G, corresponding to Cu^{2+} ions in a tetrahedral environment within the hexagonal wurtzite Cu/ZnO solid solution. There are also several small "bumps" at ~3000G that correspond to isolated superficial Cu ions on the surface.[17] In 43%$CuGaO_x$, a strong signal can be observed at 3200G. This peak corresponds to Cu^{2+} ions in the $CuGa_2O_4$ tetragonal spinel phase, in agreement with the XRD (Figure 6a). In 43%Cu−$ZnGaO_x$, this signal is still present (but trace), indicating the existence of the tetragonal spinel phase within the 43%Cu−$ZnGaO_x$ structure, as proposed from the XRD (Figure 7b); however, there is also a large, broad signal centered at ~3600G. This peak is attributed to Cu^{2+} ions in an octahedral environment within the cubic spinel structure identified from the XRD (Figure 7a). Notice that Cu^{2+} ions in CuO are EPR silent, and any Cu^+ present in the catalysts will not give an EPR signal because they are not paramagnetic.[18]

DISCUSSION

The catalytic properties of a material are intrinsically linked to its structure, since the structure plays an important role in dictating the surface area, the nature and the availability of

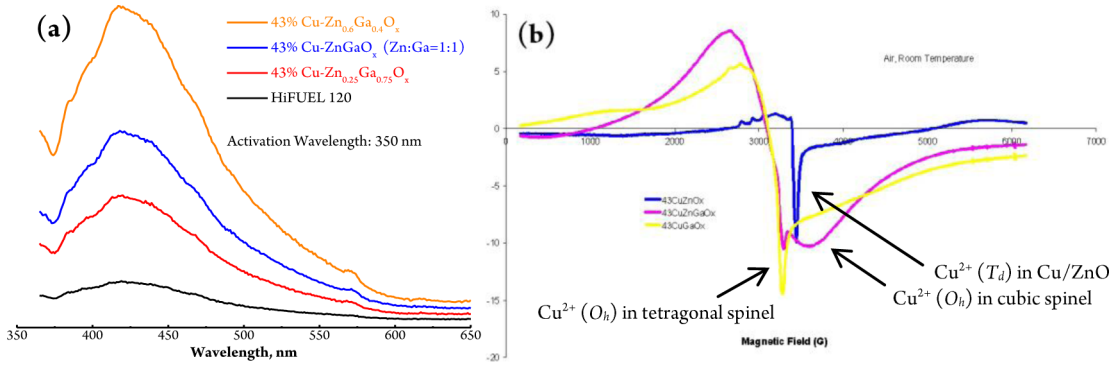

Figure 13. (a) PL spectra of $CuZnGaO_x$ with different Zn/Ga ratios in comparison with HiFUEL 120 commercial $CuZnAlO_x$ catalyst from Johnson Matthey; (b) EPR spectra for 43%$CuZnO_x$, $CuZnGaO_x$, and $CuGaO_x$.

dx.doi.org/10.1021/cs400011m | ACS Catal. 2013, 3, 1231−1244

active sites, and the strength of metal−support interactions. Our detailed composition and characterization studies clearly indicated that the addition of Ga^{3+} to Cu catalysts can give a dramatic effect to increase Cu dispersion (larger surface area and smaller Cu size), decrease CO production, and increase methanol conversion. This significant effect has not been reported before our work, which may lead to a new class of catalysts for a direct methanol steam reforming reaction at low temperature. It is therefore important to understand the associated structural changes with the incorporation of Ga^{3+} into the conventional Cu catalysts. XRD showed that the addition of Ga^{3+} can form a spinel structure with divalent metal cations in this coprecipitation process. The spinel structure, with general formula AB_2O_4, consists of a close-packed oxide. Each of the AB_2O_4 oxides contains two T_d sites and one O_h site (Figure 14). In a normal spinel, 1/8 of the T_d sites are filled by

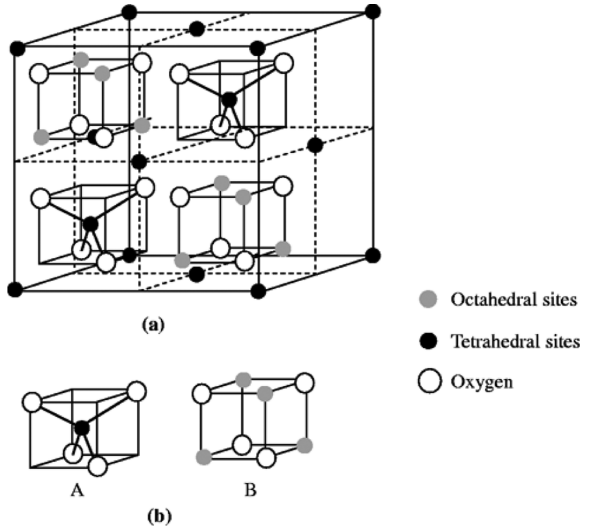

Figure 14. A cubic spinel structure, AB_2O_4[20].

A^{2+} ions and all of the O_h sites filled by B^{3+} ions. However, for Cu containing spinel, because of ligand field stabilization energy (LFSE) considerations of Cu^{2+} (d^9), Ga^{3+} (d^{10}), and Zn^{2+} (d^{10}), an inverse spinel structure is present, with Cu^{2+} occupying the O_h sites[13], Ga^{3+} filling up the T_d sites, and Zn^{2+} existing on either the T_d or O_h sites. A large degree of site swapping and substitution between Cu^{2+} and Zn^{2+} is expected within the spinel lattice as a result of the similar ionic radii of the two 2+ charged ions (neighbor elements), but in the case of $CuZnGaO_x$ mixed oxide, Cu^{2+} (d^9) in an O_h environment exhibits the Jahn−Teller effect, causing elongation and, hence, weakening of the Cu−O bonds along the axial plane. This axial distortion is what drives the formation of the tetragonal spinel phase observed in the case of $CuGa_2O_4$ without the Zn inclusion.[14] Thus, substituting Cu^{2+} for Zn^{2+} (d^{10}) is expected to help to remove this instability caused by the Jahn−Teller effect, therefore stabilizing the material in the cubic spinel phase observed for 43%Cu−$ZnGaO_x$.[19] As a result, this can account for a high degree of preference for Ga^{3+} to capture Zn^{2+} than Cu^{2+} to form the cubic spinel ions in $CuZnGaO_x$ (see EPR in Figure 13b), leaving a large excess of free Cu^{2+} (nonframework) in proximity to the spinel structure.

At elevated temperature, there may be a significant loss in structural oxygen, generating oxygen vacancies during calcination. Particularly, in spinel mixed oxide structure, the Jahn−Teller effect of particular cations (i.e., Cu^{2+}) can facilitate the removal of their axial oxygen as a result of a weaker interaction.[19,20] A typical mechanism for the formation of interstitial Cu^+ to restore electrical neutrality of the solid system is given as follows (eq 5):

$$CuGa_2O_4 \rightleftharpoons Cu_{1-2x}Cu_i^{+})_{2x}Ga_2O_{4-x} + 0.5xO_2 \quad (5)$$

Excess Cu^{2+} from CuO at the material interface may then enter the defective spinel phase to fill the vacant lattice site due to diffusion when mobile Cu^+ moves away from normal sites, forming a nonstoichiometric phase.[14]

We accept that the present proposed thermal self-reduction to form a defective spinel phase at temperatures as low as our calcination temperature may appear to be speculative because most spinels are rather stable ceramic materials and are not known to form oxygen vacancies in this low temperature range. In addition, spinels usually need a much higher temperature for their formation and are not easily obtained in an oxygen-deficient state. On the other hand, there is increasing evidence that nanosize spinels can be preferably formed at much lower temperature (room temperature formation of high-quality spinel phases with significant defects has recently been claimed[21]) due to facilitated movement of atoms at extensive interfaces.

Our characterizations, such as PL and AC impedance, indicated that the active $CuZnGaO_x$ catalyst contains a high concentration of point defects in the solid. The TPR study indicated that the Cu^+ species is present in the interstitial sites which are more reducible than Cu^{2+} and, hence, give smaller Cu clusters for higher activity at low temperature. It is thought that the small Cu clusters at the interface with defective oxide support will provide catalytically active sites for methanol and water molecule activations to H_2/CO_2 directly. The $ZnGaO_x$ defective oxide with a strong metal−support interaction with the Cu clusters can also stabilize these surface metal clusters against aggregation, hence, giving higher MSR activity. The formation of relatively large surface Cu particles from the reduction of framework Cu^{2+} (including CuO and Cu^{2+} in Cu−ZnO_x solid solution or Cu-containing spinels) would contribute to only a minor extent toward the catalytic activity as compared with those of surface Cu clusters. This explanation is consistent with the characterizations (XPS, APT, TPR, chemisorptions) that bimodal Cu sizes are obtained from the Ga-incorporated Cu/ZnO_x. We have thus identified an active type of catalyst based on $CuZnGaO_x$ that can deliver high activity and selectivity for hydrogen production from direct MSR at low temperature. Our evidence clearly suggests that Ga^{3+} incorporation in the Cu/ZnO system produces the formation of Cu^+ interstitials in the nonstoichiometric spinel phase, from which a high population of ultrafine copper clusters can be generated and stabilized during reduction at low temperature. As a result, the crucial feature for reduced CO formation is the effective interface between small Cu particles on defective oxide support, which can be created from this Ga-containing catalyst. The higher methanol steam reformation activity could be due to either the presence of these small copper islands under high isomorphic strain on the support[22,23] or the structure or morphology of the catalyst giving optimum balance between metallic Cu^0 and Cu^+ for maximum activity and selectivity.[24] It could also be assigned to highly active stepped copper particles decorated with heteroatoms (Zn or Ga atoms).[25] Further work is ongoing to elucidate the nature of the catalytically active and reaction mechanism.

dx.doi.org/10.1021/cs400011m | ACS Catal. 2013, 3, 1231−1244

SUMMARY

In summary, the in situ catalytic production of hydrogen by steam reforming of methanol at low temperature is an attractive option for use in decentralized production of clean electrical energy from PEM fuel cells. Present technologies for methanol reformation, including high-temperature steam reforming, partial oxidation, and their combination via the syn-gas route, suffer from problems that would require cumbersome CO clean-ups that, in turn, would lead to severe degradation in fuel cells' performance. In addition, there is insufficient room for such operations in portable fuel cell consumer products. Here, we report that the addition of Ga^{3+} into conventional $CuZnO_x$ catalyst by coprecipitation can facilitate the formation of a larger percentage of extremely small but more active copper clusters on a defective oxide surface, which give the higher activity for the methanol decomposition at low temperatures. At 195 °C with a longer contact time used, 43%Cu−$ZnGaO_x$ displays a high MSR activity with a small degree of CO production. However, this CO content cannot be suppressed under the reaction conditions. On the other hand, at 150 °C with a shorter contact time, the 43%Cu−$ZnGaO_x$ displays decreasing MSR activity, but this time, no detectable CO in the product gas stream is found. So far, 120 h testing has been conducted over this catalyst and we have found no deactivation under the reaction conditions. However, more prolonged testing times at vigorous conditions to evaluate the stability should be carried out.

Perhaps the important finding from this work is that under these reaction conditions, no CO formation (below 1 ppm detection limit) is observed and usable conversion of methanol to CO_2/H_2 over optimized $CuZnGaO_x$ can be achieved. As a result, this new route is technically feasible and can deliver a high quality of hydrogen gas for small mobile fuel cell devices. For further rational design of new catalysts for this reaction, it is essential to master the knowledge and skills to create such small copper clusters from nonstoichiometric Cu-containing solid structures.

EXPERIMENTAL SECTION

Catalyst Preparation. All copper-based catalysts were synthesized using a pH-controlled coprecipitation method. The precursors were hydrated metal nitrate salts, typically $Cu(NO_3)_2{\cdot}3H_2O$ (Aldrich), $Zn(NO_3)_2{\cdot}6H_2O$ (Aldrich), and $Ga(NO_3)_3{\cdot}9H_2O$ (Aldrich), each of which was dissolved completely in 100 mL of deionized water. The first batch of catalysts (Table 1, tested at 195 °C) was prepared via a simple coprecipitation method. The precursor metal nitrate salts were dissolved and combined in 100 mL of DI water, followed by a dropwise addition of aqueous Na_2CO_3 (3.50g in 100 mL of DI water) used to produce the precipitate. Both solutions were added at ~0.05 mL s^{-1} by a dropper to a round-bottomed flask containing 300 mL of DI water and a magnetic stirring bar maintained at 1500 rpm, and heated to 80−90 °C with the pH controlled at 7. The resulting precipitate was aged in solution at this temperature for 24 h. After aging, the precipitate was centrifuged 6−12 times at 6000 rpm for 5 min and washed with 50 mL of DI water between periods to remove Na^+ ions. The resulting solid was powdered, then dried in air at 80−100 °C overnight and subsequently calcined in static air, at a ramp of 3 °C min^{-1} up to 380 °C, for 180 min to produce the catalyst.

For a second batch of catalysts tested at 150 °C (Table 2), the pH of the precipitating solution was carefully maintained at 6.5 by adding a Na_2CO_3 aqueous solution (prepared by dissolving 3.50 g of Na_2CO_3 in 100 mL of DI water). A delivery pump and two 50 mL syringes were used to inject the precursor metal nitrate solution at a constant rate of 0.42 mL/min in an automatic and reproducible manner. The Na_2CO_3 solution was added using a HPLC pump at a rate of 0.5−1.0 mL/min. The solutions were added simultaneously into a plastic reactor containing 250 mL of preheated DI water and a magnetic stirring bar maintained at 1200 rpm. The precipitation process took place at around 80 °C, with the oil bath set at 100 °C. The pH was measured using a temperature-dependent pH meter and was controlled at pH 6.5, with an error range of ±0.1. Once the addition of the precursor metal nitrate solution was completed, the pH was measured again to ensure that the target pH has been proper reached before putting the lid onto the reactor. The resulting precipitate was aged in solution at 80 °C for 15 h. After aging, the precipitate was extracted by centrifugation at 4000 rpm. The centrifuged precipitate was then washed with DI water three times at 3000 rpm for 10 min to remove Na^+ ions. The resulting wet solid was dried in air at 78 °C overnight and then calcined in static air, at a ramp of 3 °C/min up to 380 °C, for 3 h to produce the final optimized catalyst.

Catalyst Testing. A self-built reactor system was set up to manipulate the reaction conditions of the methanol steam reforming reaction. Figure 15 shows the system that was used to determine the activity of the catalyst.

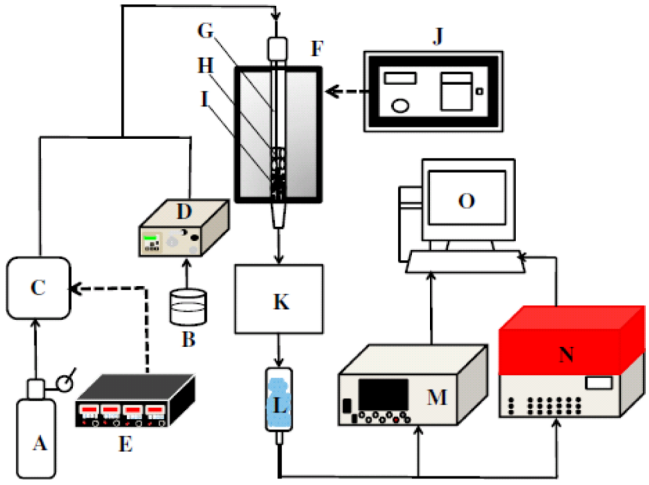

Figure 15. A reactor setup.

A 0.40 g portion of calcined catalyst and 0.40 g of silicon carbide powder were mixed thoroughly and inserted into a 4-mm-diameter silica reactor (G). The powder mixture was sandwiched between silica wool plugs (I). The silica reactor (G) was wound with a thermocouple that connected the reactor to the temperature-programmable furnace (J and F). Before testing, the catalyst was pretreated with a gas stream of <10% N_2 at 20 mL/min and a H_2 gas stream at 10 mL/min from room temperature up to 150 °C for 2.5 h. After the pretreatment, the testing started with a flow of methanol/water solution (B), which had a CH_3OH/H_2O ratio of 1:2, pumping from the HPLC pump (D) at a flow rate of 0.1 mL/min. A N_2 gas stream (A), controlled by a mass-flow controller (C and E), was injected simultaneously with the methanol/water solution at a flow rate of 10 mL/min. All liquids in the methanol, water, and nitrogen mixture were fully converted into gas by passing

dx.doi.org/10.1021/cs400011m | ACS Catal. 2013, 3, 1231−1244

through the preheated tubing maintained at 150 °C before arriving at the reactor. A preweighed two-necked flask was placed in a dry ice bath (K and L) to remove excess water and methanol from the reacted mixture. After passing through the dry ice cold trap, the remaining product gas stream reached the precalibrated gas chromatography with a thermal conductivity detector (M). The quantity of each individual gas in the product, including H_2, CO, CO_2, N_2, and CH_4, could then be determined and analyzed using the computer (O). For the CO level analysis, a separated FID (N) with a detection limit of 10 ppm was used because the GC was not sensitive enough.

The synthesized catalysts were tested under the steam-reforming condition; their activity and conversion properties were then calculated. We derived the methanol conversion and product selectivity from product gas analysis (CO_2, CO, H_2, N_2, etc.) for each run using calibration. However, actual methanol analysis with the correlation to the value derived from the analysis of the product gases was regularly checked by comparing the quantity of methanol collected at the condenser and at the beginning tube to make sure the all calibrations were correct. The CO concentration was directly measured using the calibrated GC and FID.

$$\text{CH}_3\text{OH conversion (\%)} = \frac{\{[\text{CH}_3\text{OH}]\text{in} - [\text{CH}_3\text{OH}]\text{out}\}}{[\text{CH}_3\text{OH}]\text{in}} \times 100$$

TPR. Temperature-programmed reduction (TPR) measurements were obtained using a ThermoQuest TPRO 110 instrument. Inside the TPR quartz tube, 0.026 g of the calcined catalyst sample was sandwiched between two layers of glass wool with a thermocouple placed in contact with the sample. The TPR tube was then inserted into the instrument for a helium pretreatment. The helium gas pretreatment (He running through the TPR tube at 10 mL/min at a temperature ramp of 10 °C/min from 40 to 150 °C, then held for 5 min before cooling) cleaned the catalyst surface by removing any absorbed ambient gas molecules. After the pretreatment, a reduction treatment (5% H_2 in argon flowing through the TPR tube at 20 mL/min at a temperature ramp of 10 °C/min from 40 to 330 °C, then held at 330 °C for 30 min before cooling to room temperature) was carried out to reduce the Cu^{2+} within the sample. $Cu^{(II)}O$ was reduced to Cu^0 by the flow of hydrogen gas in the reduction treatment. The consumption of hydrogen gas changed the conductivity of the gas stream; hence, the change in conductivity was measured and calibrated as a function of both temperature and time to produce the TPR profile.

Chemisorption. The reduction treatment of Cu^{2+} to Cu^0 in the catalyst sample (first TPR) was followed by N_2O chemisorption at room temperature to determine the size of copper metal particles. Treatment with 5% N_2O/Ar at 20 mL/min for 40 min was carried out to reoxidize only the Cu surface via dissociative chemisorption. To remove any remaining adsorbed N_2O, another He pretreatment (He flowing at 10 mL/min for 10 min at RT) was carried out. This was followed by a second reduction treatment (second TPR: 5% H_2 in argon at 20 mL/min at a temperature ramp of 10 °C/min from 40 to 330 °C). By analyzing data from the first and second TPR, it was possible to determine the Cu surface area of the catalyst sample by precalibrating the TPR with a $Cu^{(II)}O$ standard of known Cu content. Standard samples of $Cu^{(II)}O$ (0.005, 0.0010, and 0.0015g (Aldrich)) were used to perform the TPR, and the number of moles of hydrogen consumed was calculated. The result was then plotted against the TPR integrated peak area to give a first-order calibration plot. The Cu dispersion is defined as the fraction of Cu atoms exposed to the surface. It was calculated as follows:

$$D_{\text{Cu}} = \frac{N_{\text{surface}}}{N_{\text{total}}} = \frac{\text{surface CuH}_2\text{ consumption (2nd TPR)}}{\text{total CuH}_2\text{ consumption (1st TPR)}} \times 100\%$$

The specific Cu metal surface area of the catalyst was calculated as

$$\text{SA}_{\text{cat}} = \frac{\text{surface Cu atoms g}^{-1}\text{ cat}}{\text{surface Cu packing density}} \quad (\text{units} = \text{m}^2\,\text{g}^{-1}\,\text{cat})$$

The specific Cu metal surface area of Cu in the catalyst was calculated as

$$\text{SA}_{\text{Cu}} = \frac{\text{SA}_{\text{cat}}}{\text{Cu loading of catalyst}} \quad (\text{units} = \text{m}^2\,\text{g}^{-1}\,\text{Cu})$$

The Cu particle size was calculated as being the average diameter of the Cu particles on the surface, assuming spherical geometry.

$$X_{\text{Cu(nm)}} = \frac{6 \times 10^9}{\text{SA}_{\text{Cu}} \times \text{Cu}_{\text{density}}}$$

(NB: The above calculations are valid only by making the assumption that N_2O is decomposed to N_2, with the simultaneous oxidation of surface Cu to Cu_2O.)

XRD. The X-ray diffraction (XRD) profile was collected by a Philips PW-1729 diffractometer with Bragg−Brentano focusing geometry using Cu Kα radiation (λ = 1.5418 Å) from a generator operating at 40 kV and 40 mA.

HAADF−STEM. Both bright field imaging and high-angle annular dark field scanning transmission electron microscopy (HAADF−STEM) were used to investigate the structure of the Cu-based catalyst materials after reduction. Using these imaging techniques, an aberration-corrected transmission electron microscope can reveal small Cu particles with a high contrast (bright spots) from the background.

APT. Samples were analyzed for APT using a pulsed laser mode (0.45 nJ energy, 10 μm spot size, 160 kHz repetition rate) at a specimen temperature of 55 K. Cu-containing catalyst nanoparticles were first deposited onto a preformed, needle-shaped Pt−Rh atom probe that was preelectropolished in a molten salt mixture (4:1 $NaNO_3$/NaCl) starting from platinum-22 atom % rhodium wire (0.1 mm diameter, Alfa-Aesar). Using stock solutions of nanoparticles in methanol, a droplet was placed in a gold electropolishing loop, and a voltage bias was applied between the loop and the Pt−Rh specimen. On dipping the needle into the loop, nanoparticles were drawn through the potential gradient by electrophoresis toward the apex region, where they subsequently attached. Each sample was then inspected using a transmission electron microscope (Phillips CM20) to confirm nanoparticle deposition. The variables of particle type, size, and polarity, along with specimen sharpness and dipping duration, all affect the deposition process and had to be carefully explored. Exposing the specimens for longer periods in the nanoparticle solution allowed further deposition, but the larger degree of agglomeration of particles

dx.doi.org/10.1021/cs400011m | ACS Catal. 2013, 3, 1231−1244

was difficult to analyze at a later time. Typical conditions to deposit a thin layer of Cu nanoparticles were 5−15 V, applied for ∼10 s of total current flowing, using a Pt−Rh needle of ∼40−50 nm end radius. Once deposited and checked in the TEM, each sample was transferred to the storage chamber (Cameca LEAPTM 3000HR) to minimize contamination before the APT measurement.

XPS. X-ray photoelectron spectroscopy (XPS) was used to conduct surface and near-surface chemical analysis. After reduction, samples were carefully transferred in a glovebag without air exposure and analyzed by XPS. A typical survey scan of $CuZnGaO_x$ was first collected to verify the catalyst composition, and the binding energy for the Cu 2p 3/2 peak before and after reduction was then collected with higher accuracy.

AC Impedance. The impedance of a material describes its resistance to alternating current. It is represented by the complex quantity, Z. By plotting the real component (resistance, $Z1$) versus the imaginary component (reactance, $Z2$) of a material's impedance across a range of frequencies, we obtain a semicircular spectrum known as a Nyquist plot. By obtaining such spectra over a range of temperatures, it is possible to gain information about the charge-carrying properties of the material. In the case of the present study, the predominant mechanisms for electrical conductivity within the calcined catalyst materials are either via mobile Cu ions, in which Cu is able to move between either substitutable lattice sites or interstices, or via oxygen mobility, where O^{2-} anions are able to "hop" into adjacent vacant lattice sites. These processes have associated thermal activation energies, which describe the ease with which a mobile ion can move between sites. To obtain the impedance measurements over a range of temperatures, the calcined catalyst was pressed at 5 tons of pressure into a pellet of approximately 1 mm thickness and 30 mm diameter, then held between two platinum electrodes inside a quartz tube containing a thermocouple and wrapped in an electrical thermal jacket attached to a programmable heating furnace. The electrodes were connected to an Ivium CompactStat electrochemical interface, which in turn was connected to a PC with the corresponding IviumSoft software. For each material studied, the sample was heated to 220 °C and maintained at that temperature for 1 h, then allowed to cool by 20° increments and held at each temperature for 20 min before taking a measurement. The frequency range used was from 100 000 to 2 Hz, the current range was 100 μA, and the frequency scan amplitude was 0.5 V.

EPR Spectroscopy. Samples were characterized by electron paramagnetic resonance (EPR) using a Bruker EMX X-band CW spectrometer and a 100 mg solid sample in a quartz tube. In the presence of an external magnetic field ($\mathbf{B}_0$), the electrons within a material will align their magnetic moments either parallel (ms = −1/2) or antiparallel (ms = +1/2) to the applied field. These alignments have different energies, and the phenomenon is known as the Zeeman effect. The separation between the energy states can be written in terms of the g-factor (g_e) and the Bohr magneton (μB):

$$\Delta E = E + 1/2 - E - 1/2 = g_e \mu_B B_0$$

Unpaired electrons within the material can move between the energy levels by absorbing a photon that satisfies the resonance condition:

$$h\nu = g_e \mu_B B_0$$

The statistical distribution of unpaired electrons within a paramagnetic sample is described by the Boltzmann distribution:

$$\frac{n_{\text{upper}}}{n_{\text{lower}}} = e^{-h\nu/kT}$$

In practice, there will be a slightly larger population in the lower energy state than the upper one. This means that in an external magnetic field, there will be a net absorption of energy because transitions from the lower to upper state are more probable. This net absorption is measurable and forms the basis of EPR spectroscopy. The g-factor depends not only on the external magnetic field but also on local fields within the material; therefore, by measuring the g-factor, it is possible to investigate species in different electronic environments. The electronic environment of paramagnetic transition metal ions such as Cu^{2+} in the Cu/Zn/Ga oxide system may be investigated using EPR. By looking at the electronic environments of the Cu ions, we may be able to distinguish between different lattice sites and possibly identify the most active site for the steam reforming reaction by the EPR.

■ ASSOCIATED CONTENT

Ⓢ Supporting Information

Supporting Information for this paper is available. This information is available free of charge via the Internet at http://pubs.acs.org/.

■ AUTHOR INFORMATION

Corresponding Author

*E-mail: edman.tsang@chem.ox.ac.uk.

Present Address

†Shanghai Research Institute of Petrochemical Technology, SINOPEC, Shanghai 201208, China.

Notes

The authors declare no competing financial interest.

■ ACKNOWLEDGMENTS

EPSRC, UK (EP/G01244X/1, under SUPERGEN consortium, Delivery of Sustainable Hydrogen (DoS)). This work was funded by EPSRC, UK. The authors thank Dr. Jingping Hu and Prof. John Foord of Oxford Chemistry for XPS; Dr. Tong Li and Prof. George Smith of Oxford Materials for APT; and Prof. Heyong He of Fudan University, P.R. China for HAADF-STEM. We also thank Drs. Martin Fowles and Colin Park of Johnson Matthey, U.K. for useful discussion. W.T. acknowledges the China Scholarship Committee (CSC) and permission from ECUST to undertake research at Oxford University.

■ REFERENCES

(1) *Kyoto Protocol to the United Nations Framework Convention on Climate Change*, 1998; Online at http://unfccc.int/resource/docs/convkp/kpeng.pdf

(2) *UK Climate Change Act*, 2008; Online at http://www.legislation.gov.uk/ukpga/2008/27/contents

(3) Schmidt, T. J.; Gasteiger, H. A.; Behm, R. J. *Electrochem. Commun.* **1999**, *1*, 1.

(4) Patil, A. S.; Dubois, T. G.; Sifer, N.; Bostic, E.; Gardner, K.; Quah, M.; Bolton, C. *J. Power Sources* **2004**, *136*, 220.

(5) Tedsree, K.; Li, T.; Jones, S.; Chan, C. W. A.; Yu, K. M. K.; Bagot, P.; Marquis, E.; Smith, G.; Tsang, S. C. E. *Nat. Nanotechnol.* **2011**, *6*, 302.

(6) Palo, D. R.; Dagle, R. A.; Holladay, J. D. *Chem. Rev.* **2007**, *107*, 3992.
(7) Olah, G. A.; Coeppert, A.; Prakash, G. K. S. *Beyond Oil and Gas: The Methanol Economy*, 2nd ed.; Wiley-VCH: Los Angeles, CA, USA, 1998.
(8) Sun, H.-N.; Exxon Mobil; Patent WO98/29333/PCT/US97/24124.
(9) Sá, S.; Silva, H.; Brandão, L.; Sousa, J. M.; Mendes, A. *Appl. Catal., B* **2010**, *99*, 43.
(10) Yu, K. M. K.; Tong, W.; West, A.; Cheung, K.; Li, T.; Smith, G.; Guo, Y.; Tsang, S. C. E. *Nat. Commun.* **2012**, *3*, 1230 DOI: ; 10.1038/ncomms2242.
(11) Zhu, J.; Gao, Q. *Microporous Mesoporous Mater.* **2009**, *124*, 144.
(12) Kumekawa, Y.; Hirai, M.; Kobayashi, Y.; Endoh, S.; Oikawa, E.; Hashimoto, T. *J. Therm. Anal. Calorim.* **2009**, *99*, 57.
(13) Payer, A.; Schöllhorn, R.; Ritter, C.; Paulus, W. *J. Alloys Compd.* **1993**, *191*, 37.
(14) Biswas, S. K.; Sarkar, A.; Pathak, A.; Pramanik, P. *Talanta* **2010**, *81*, 1607.
(15) Crescenzi, M. D.; Diociaiuti, M.; Lozzi, L.; Picozzi, P.; Santucci, S. *Surf. Sci.* **1986**, *178*, 282.
(16) Jochum, W.; Penner, S.; Föttinger, K.; Kramer, R.; Rupprechter, G.; Klötzer, B. *J. Catal.* **2008**, *256*, 268.
(17) Cordoba, G.; Viniegra, M.; Fierro, J. L. G.; Padilla, J.; Arroyo, R. *J. Solid State Chem.* **1998**, *138*, 1.
(18) McKinnon, W. R.; Morton, J. R.; Pleizier, G. *Solid State Commun.* **1988**, *66*, 1093.
(19) Guisnet, M. Heterogeneous Catalysis and Fine Chemicals III: Proceedings of the 3rd International Symposium, Poitiers, April 5−8, 1993, p 275
(20) Shapovalov, V. A.; Szymezak, H.; Piechota, S.; Shapovalov, V. V. *J. Phys. IV France* **1997**, *7*, C1.
(21) Cheng, F.; Shen, J.; Peng, B.; Pan, Y.; Tao, Z.; Chen, J. *Nat. Chem.* **2011**, *3*, 79.
(22) Kasatkin, I.; Kurr, P.; Kniep, B.; Trunschke, A.; Schlögl, R. *Angew. Chem., Int. Ed.* **2007**, *46*, 7324.
(23) Ressler, T.; Kniep, B. L.; Katsatkin, I.; Schlogl, R. *Angew. Chem., Int. Ed.* **2005**, *44*, 4704.
(24) Ritzkopf, I.; Vukojević, S.; Weidenthaler, C.; Grunwaldt, J.-D.; Schüth, F. *Appl. Catal., A* **2006**, *302*, 215.
(25) Behrens, M.; Studt, F.; Kasatkin, I.; Kühl, S.; Hävecker, M.; Abild-Pedersen, F.; Zander, S.; Girgsdies, F.; Kurr, P.; Kniep, B.-L.; Tovar, M.; Fischer, R. W.; Nørskov, J. K.; Schlögl, R. *Science* **2012**, *336*, 893.